ROYAL SOCIETY
OF CHEMISTRY

PAPER

Check for updates

Sublimable complexes with spin switching: chemical design, processing as thin films and integration in graphene-based devices†

Miguel Gavara-Edo, ‡[a] Francisco Javier Valverde-Muñoz, ‡[a] Rosa Córdoba, [a]
M. Carmen Muñoz, [b] Javier Herrero-Martín, [c] José Antonio Real *[a] and
Eugenio Coronado *[a]

Among the different types of switchable molecular compounds, sublimable Fe(II) SCO molecules provide a suitable platform to develop smart devices that respond to external stimuli. Herein, we report the synthesis, crystallographic structure and magnetic properties of three new neutral Fe(II) SCO molecules belonging to the {Fe[H$_2$B(pz)$_2$]$_2$(L)} family with bidentate-α-diimine ligands L = 3-(pyridin-2-yl)-[1,2,3]triazolo[1,5-a]pyridine (tzpy), 5,5′,6,6′-tetrahydro-4H,4′H-2,2′-bi(1,3-thiazine) (btz) and 4,4′,5,5′-tetrahydro-2,2′-bithiazole (bt) (**1**, **2** and **3**, respectively), as well as two solvated forms of **1** and **3**. All three desolvated compounds present thermal- and light-induced SCO transitions with different degrees of cooperativity and effectiveness. Furthermore, **1** and **2** are demonstrated to be sublimable under HV conditions, affording homogeneous thin films 200 nm thick (**TF1** and **TF2**) that retain the chemical integrity of the original molecules regardless of the deposition surface. The SCO behaviour of the films is characterized by the XAS technique revealing the partial retainment of both thermal- and light-induced spin transitions, yet losing the cooperativity. Finally, SCO/2D horizontal hybrid devices based on CVD-graphene are produced using these films. Being the first ones of this type utilizing molecules of the {Fe[H$_2$B(pz)$_2$]$_2$(L)} family, with L = tzpy and btz, the devices have allowed the successful detection of the thermal SCO transition through the electric properties of CVD-graphene.

10th Anniversary statement

Since the splitting of *Journal of Materials Chemistry* into three *A*, *B* and *C* independent journals, these journals have reached a much broader range of scientific communities. Nowadays, these journals constitute one of the best platforms for exchanging and disseminating knowledge within the multidisciplinary field of materials chemistry. In our case, we have published in these journals more than 40 articles mostly based on multifunctional molecular materials exhibiting appealing magnetic, optical and electrical properties and showing potential for different applications. Thanks to the *J. Mater. Chem.* family of journals, we have been able to contribute to the development of emerging fields such as molecular spintronics and molecular quantum technologies. For this and for much more, congratulations!.

[a] *Institute of Molecular Science, University of Valencia, Catedrático José Beltrán 2, Paterna 46980, Spain. E-mail: Jose.A.Real@uv.es, Eugenio.Coronado@uv.es*

[b] *Departamento de Física Aplicada, Universitat Politècnica de València, Camino de Vera s/n, Valencia 46022, Spain*

[c] *Boreas Beamline CELLS-ALBA Synchrotron, Carrer de la Llum 2-26, Cerdanyola del Vallès 08290, Spain*

Introduction

Octahedral Fe^{II} spin crossover (SCO) complexes are molecular materials that reversibly switch between high-spin (HS: t$_{2g}^4$e$_g^2$, $S = 2$) and low-spin (LS: t$_{2g}^6$e$_g^0$, $S = 0$) states inducing changes in the magnetic, optical, electrical and structural properties controlled through the action of external stimuli such as temperature and/or pressure changes, light irradiation and guest molecules. These features have attracted much attention due to their potential applicability as active components in electronic and spintronic devices, *e.g.* sensors and memory devices.[1–9] To this end, selected Fe^{II} SCO materials have been processed at

sub-micrometer scales as nanocrystals/nanoparticles or also as thin films usually deposited by layer-by-layer or high-vacuum (HV) sublimation methods.[10,11]

HV sublimation has been demonstrated to be an efficient method to grow very pure films of SCO nanomaterials with a sub-monolayer precision. This has been demonstrated for a reduced number of neutral mononuclear Fe^{II} SCO complexes affording intermolecular interactions that favour sublimation under relatively mild conditions. Among them, [Fe(phen)$_2$(NCS)$_2$],[12–14] {Fe[H$_2$B(pz)$_2$]$_2$(L)}[15–17] with L = phen and bipy ([H$_2$B(pz)$_2$]$^-$ = hydrobispyrazolylborate, L = 1,10-phenanthroline, 2,2′-bypiridine) and [Fe(Pyrz)$_2$][18,19] (Pyrz = hydro-tris-(3,5-dimethyl-pyrazolyl)borate) have been most investigated. To the best of our knowledge, the first thin films based on SCO molecules deposited by sublimation were reported in the last decade for the archetypal [Fe(phen)$_2$(NCS)$_2$].[20] More recently, this study was extended to investigate the effect of different metallic substrates on the SCO properties of this molecule.[21] However, thin films of the complex {Fe[H$_2$B(pz)$_2$]$_2$(phen)} deposited on different substrates have been the most intensively investigated. These studies have revealed electron-induced reversible switching of single SCO complexes[22] and the light induced excited spin state trapping (LIESST) phenomenon on ultrathin films deposited on Au(111),[23] also on highly oriented pyrolytic graphite (HOPG) surfaces,[24] and even electrically sensed when embedded in a vertical junction.[25] In addition, they have inspired the preparation of homologous complexes derived from the 4-methyl-/-chloro- and 4,7-dimethyl-/-dichloro substituted phen,[26] whose SCO properties have been investigated in bulk and thin films by sublimation on HOPG and for the 3,4,7,8-tetramethyl homologous complexes deposited on Au(111) and bismuth.[27] Concerning {Fe[H$_2$B(pz)$_2$]$_2$(bipy)}, it has been observed the locking and unlocking of the SCO behavior as a function of the film thickness on Au(111), or deposited on dielectric substrates (SiO$_2$ and Al$_2$O$_3$).[28–30] Also, a practically complete SCO transition has been observed on HOPG, showing a clear growth of cooperativity with the increase of the number of monolayers from 0.35(4) to 10(1).[31] A different approach to explore cooperativity has been used preparing 10 nm thin films of the sublimed {Fe[H$_2$B(pz)$_2$]$_2$(bipy*)} system on SiO$_2$, bipy* being a 2,2′-bipyridine functionalized with a dodecyl (C_{12}) alkyl chain to favour intermolecular interactions.[32] Lately, much effort has been dedicated to study the sublimation of [Fe(Pyrz)$_2$]. At first, when processed as thin films (ca. 100 nm thick regime), this system was observed to present an incomplete thermal SCO transition, yet in a similar temperature range to that of the bulk material without clear loss of cooperativity.[33] Furthermore, both LIESST and soft X-ray induced excited spin state trapping (SOXIESST), known to occur in the bulk, were as well found in the films. Subsequent work revealed the coexistence of two polymorphs within the sublimed films of this molecule, where each of them appears to present a different SCO behaviour.[34] Then, using the most stable polymorph, a spin-state device was first produced incorporating this molecule.[35] More recently, further work was devoted in this direction by exploiting the more effective light-induced SCO properties of the less stable polymorph with its integration in a first-of-its-kind contactless graphene-based horizontal device.[36] In parallel, ultrathin films (submonolayers) of this molecule have been studied on different substrates showing that they experience a variety of surface induced effects such as electric field induced HS/LS ordered superstructures, quenching of the HS state, a reverse LIESST effect, single-molecule spin state manipulation and negative differential resistance.[37–43] All these studies have evidenced the vast and rich SCO phenomenology available for each of the different molecular systems aforementioned. Nonetheless, it should be noted that other sublimable SCO molecules have been reported as well such as {Fe[HB(pz)$_3$]$_2$},[44,45] {Fe[HB(trz)$_3$]$_2$},[46] [Fe(dpepd)(NCS)$_2$],[47] [Fe(qnal)$_2$]·xCH$_2$Cl$_2$,[48] and [Fe(pypyr(CF$_3$)$_2$)$_2$(phen)][49] (all the ligands corresponding to these molecules are depicted in Scheme 1).
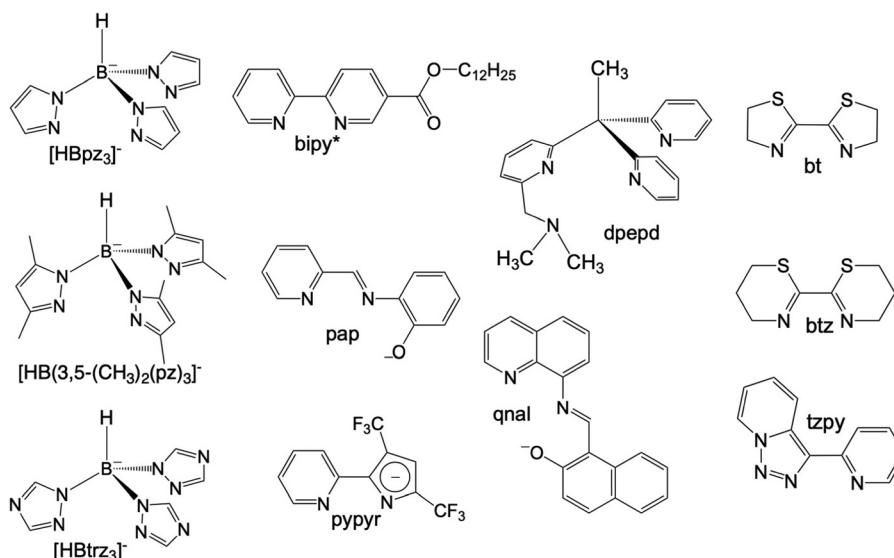
Scheme 1 Selection of ligands used in the preparation of sublimable Fe^{II} complexes (see the text).

8108 | *J. Mater. Chem. C*, 2023, **11**, 8107–8120

This journal is © The Royal Society of Chemistry 2023

In this context, here we describe the synthesis, structure, magnetic and photomagnetic properties for the bulk materials of three new SCO molecules of the $\{Fe[H_2B(pz)_2]_2(L)\}\cdot nS$ type, with L being the bidentate-α-diimine ligands tzpy (**1·CH₃CN**, **1**), btz (**2**), and bt (**3·1/2CH₂Cl₂**, **3**) (see Scheme 1). Furthermore, we have succeeded in the preparation of thin films **TF1** and **TF2** deposited on different substrates (SiO₂, Au coated (40 nm) glass and CVD-graphene) from sublimation under HV conditions of the as-synthesized **1** and **2** bulk powders, respectively, probing their sublimable character. In contrast, **3** has been found to decompose upon heating under HV conditions without sublimation. The chemical integrity of **TF1** and **TF2** has been analyzed by means of infrared (IR) and Raman spectroscopies, while their thermal and light-induced SCO behavior has been monitored by means of X-ray absorption spectroscopy (XAS). Finally, **TF1** and **TF2** films have been integrated on horizontal hybrid devices based on CVD-graphene to detect the thermal SCO behavior of the films through the electrical properties of the 2D material, since graphene has been previously proven as a highly sensitive platform to the changes undergone by SCO materials upon their spin transition (*i.e.* devices based on sublimed films and van der Waals heterostructures).[35,36,50]

Results and discussion

Synthesis

$\{Fe[H_2B(pz)_2]_2(L)\}$ (L = btz, tzpy and bt) complexes were synthesized following the method previously described for L = phen and bipy.[15] Under the reported conditions, $\{Fe[H_2B(pz)_2]_2(tzpy)\}$ is rapidly formed giving a pink-orange microcrystalline precipitate (**1**). Single crystals of its acetonitrile solvate (**1·CH₃CN**) were isolated in 48 h from liquid-to-liquid layering of a MeOH solution of $[Fe^{II}/2[H_2B(pz)_2]^-]$ (bottom) and a CH₃CN solution of tzpy (top) separated by a mixture of MeOH:CH₃CN. The thermal analysis of the resulting needle-shaped crystals shows a sharp loss of weight in the interval 390–410 K consistent with a mol of CH₃CN per mol of complex (Fig. S1a, ESI†). Powder X-ray diffraction patterns show that the desolvated form corresponds to the pink-orange microcrystalline phase (**1**) (Fig. S1b,

ESI†). Compound $\{Fe[H_2B(pz)_2]_2(btz)\}$ (**2**) precipitates as a deep blue highly crystalline product of medium solubility, while single crystals for appropriate structure analysis were obtained within 24 h from evaporation of the resulting methanolic mother liquor under an Ar stream. The same synthetic procedure used for L = bt gave single crystals of the unsolvated complex $\{Fe[H_2B(pz)_2]_2(bt)\}$ (**3**). However, given the relative low solubility of bt in MeOH and in order to increase the yield of the complex, CH₂Cl₂ was used as an alternative solvent where bt is more soluble, thereby affording the corresponding hemisolvate form (**3·1/2CH₂Cl₂**). The thermal analysis shows that a loss of weight, consistent with one molecule of CH₂Cl₂ per two moles of complex, takes place in the temperature interval 379–450 K (Fig. S2, ESI†).

Magnetic properties

The magnetic properties were monitored through the thermal dependence of the product $\chi_M T$ with χ_M being the molar magnetic susceptibility and T being the temperature. The $\chi_M T$ *vs. T* plots for the solvate and unsolvate form of the tzpy derivative are shown in Fig. 1a. At 300 K, the $\chi_M T$ value is *ca.* 3.80 cm³ K mol⁻¹ for **1** and **1·CH₃CN**. This value decreases by *ca.* 0.3 cm³ K mol⁻¹ upon cooling down to 180 K (**1**) and 200 K (**1·CH₃CN**). Below these temperatures, both forms show a complete HS-to-LS transformation reaching a $\chi_M T$ value of about 0.1 cm³ K mol⁻¹ at 50 K. The SCO takes place, respectively, in one and two steps for the **1·CH₃CN** and **1**, being more cooperative for the latter. Indeed, in the heating mode, the $\chi_M T$ *vs. T* plot matches quite well the cooling mode for the **1·CH₃CN** form but a very narrow hysteresis (*ca.* 4 K) is observed for **1**. The equilibrium temperature $T_{1/2}$ at which the HS and LS molar fractions are equal to 0.5 is 135 K (**1·CH₃CN**) and 167.5 K (**1**), respectively. For the latter, the characteristic temperatures at which the $[\partial(\chi_M T)/\partial T]$ *vs. T* plot shows a maximum are 157 and 177 K.

For compound **2**, the $\chi_M T$ value is 3.7 cm³ K mol⁻¹ at 300 K and decreases slightly upon cooling down to 210 K (Fig. 1b). Just below this temperature, it undergoes a cooperative one step SCO transition attaining a $\chi_M T \approx 0$ cm³ K mol⁻¹ at 192 K. In the heating mode, the $\chi_M T$ *vs. T* plot does not match that of
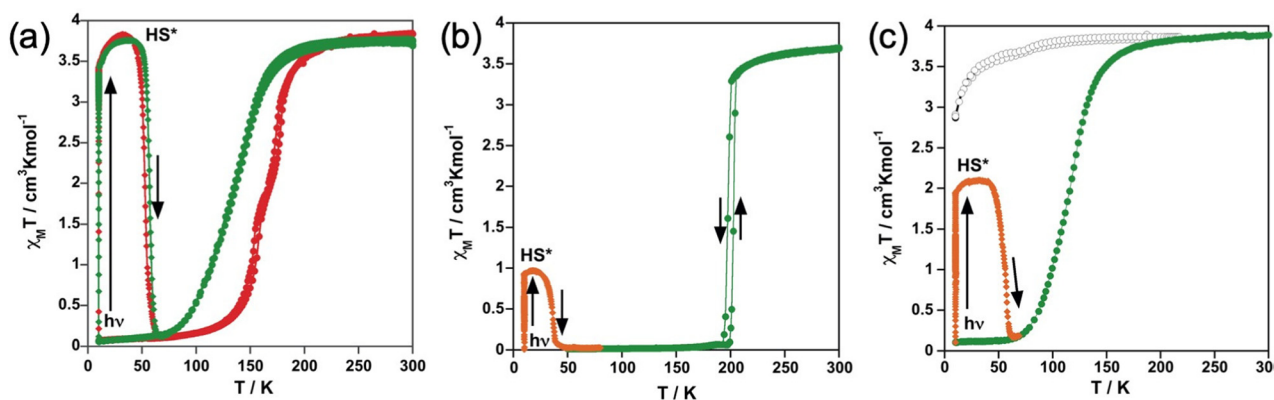

Fig. 1 Magnetic and photomagnetic properties for (a) **1** and **1·CH₃CN** red and green solid circles, respectively; (b) **2** (green solid circles) and (c) **3·1/2CH₂Cl₂** (green solid circles) and **3** (black open circles).

the cooling mode defining a hysteresis loop 6 K wide with $(T_{1/2})^{down}$ = 197 K and $(T_{1/2})^{up}$ = 203 K.

Concerning compound **3**, the $\chi_M T$ value 3.8 cm^3 K mol^{-1} remains almost constant down to 50 K and then slightly decreases due to the occurrence of zero-field-splitting of the S = 2 HS state denoting the stabilization of the HS state at all temperatures. In contrast, for the solvate form **3·1/2CH$_2$Cl$_2$**, $\chi_M T$ decreases as T decreases in a very similar way as described for the solvate form of the tzpy, **1·CH$_3$CN**, undergoing a complete SCO characterized by $T_{1/2}$ = 116 K (Fig. 1c).

Photo-generation of the metastable HS* state from the LS state, the so-called LIESST experiment,[51] was carried out at 10 K irradiating microcrystalline samples of the title compounds with green light (λ = 532 nm). Under these conditions, the four samples that display SCO undergo the LIESST phenomenon with different yields. Indeed, $\chi_M T$ saturates to values of 3.4 cm^3 K mol^{-1} for **1** and **1·CH$_3$CN**, 1.9 cm^3 K mol^{-1} for **3·1/2CH$_2$Cl$_2$** and 0.9 cm^3 K mol^{-1} for **2**. Subsequently, the light was switched off and the temperature increased at a rate of 0.3 K min^{-1} inducing a gradual increase of $\chi_M T$ that attains a maximum value of 3.8 cm^3 K mol^{-1} in the interval of 30–35 K for **1** and **1·CH$_3$CN**, 2.09 cm^3 K mol^{-1} for **3·1/2CH$_2$Cl$_2$** in the interval 20–30 K, and 0.97 for **2** at 17 K, which corresponds,

respectively, to *ca.* 100%, 54% and 26% of the maximum value observed at 300 K. This increase in $\chi_M T$ reflects the thermal population of different microstates originating from the zero-field splitting of the HS* state. At higher temperatures, $\chi_M T$ decreases rapidly until joining the thermal SCO curve, respectively, at *ca.* 65, 63 and 47 K, indicating that the metastable HS* state has relaxed back to the stable LS state. The corresponding T_{LIESST} temperatures, evaluated as $\partial(\chi_M T)/\partial T$,[52] are, respectively, *ca.* 55, 57 and 36 K. These temperatures are consistent with the inverse-energy-gap law, *i.e.* the metastability of the photogenerated HS* species decreases as the stability of the LS increases.[53–55]

Structure

Single crystals of **1·CH$_3$CN**, **2**, **3·1/2CH$_2$Cl$_2$** and **3** were measured, respectively, at 110 K/250 K, 120 K/240 K, 120 K/220 K and 120 K. The crystals keep the same space group at both temperatures, **1·CH$_3$CN** (triclinic $P\bar{1}$), **2** (orthorhombic $Pna2_1$) and **3·1/2CH$_2$Cl$_2$** (monoclinic $P2_1/c$). The unsolvate form **3** adopts the triclinic $P\bar{1}$. Selected crystal data are gathered in Table S1 (ESI†).

The molecular structure for the four derivatives is depicted in Fig. 2 together with the atom numbering. The Fe^{II} centre is surrounded by two [H$_2$B(pz)$_2$]$^-$ anionic ligands adopting each

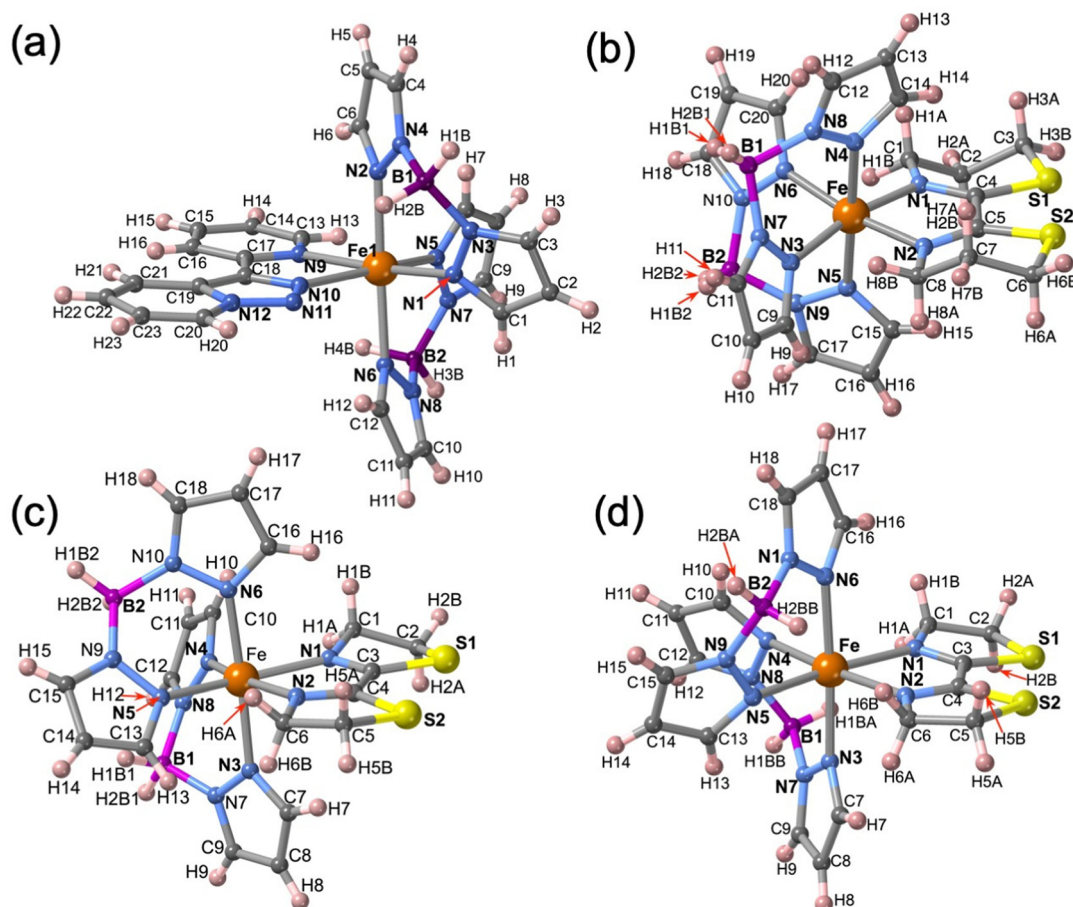Fig. 2 Molecular unit of **1·CH$_3$CN**, **2**, **3·1/2CH$_2$Cl$_2$** and **3**, showing the atom numbering. Only one of the two Fe^{II} centres (Fe1) is shown in **1·CH$_3$CN**, for Fe2 (see Fig. S3, ESI†).

other a *cis* conformation, while the remaining positions are occupied by the bidentate-α-diimine ligand L = tzpy, btz or bt, thereby completing a distorted [FeN$_6$] octahedral geometry with the Fe–N bond lengths defined by the [H$_2$B(pz)$_2$]$^-$ ligands shorter than those defined by L. A selection of significant bond-lengths and angles is gathered in Tables S2–S6 (ESI†). Furthermore, the complexes are chiral but both enantiomers coexist in the unit cell. Two slightly different Fe sites (Fe1 and Fe2) and consequently four crystallographically distinct [H$_2$B(pz)$_2$]$^-$ ligands are found for **1·CH$_3$CN** (only the Fe1 site is displayed in Fig. 2a, site Fe2 is shown in Fig. S3, ESI†). At 250 K, the average bond lengths ⟨Fe1–N⟩ = 2.188(3) Å and ⟨Fe2–N⟩ = 2.187(3) Å are practically identical. However, at 110 K, both sites exhibit an unsymmetrical decrease of ⟨Fe–N⟩ as the LS state is populated: ⟨Fe1–N⟩ = 2.018(6) Å and ⟨Fe2–N⟩ = 2.058(6) Å, which involves a change in ⟨Fe1–N⟩ and ⟨Fe2–N⟩ of 0.170 and 0.129 Å, respectively. Taking into account a structural reinvestigation of the L = phen and bipy homologous complexes, the ⟨Fe1–N⟩ change is 0.180 Å,[17] and assuming this value applicable to the title compounds, a transformation of 95% and 71% is found for Fe1 and Fe2 sites, respectively. Considering the two Fe sites, the overall transformation is 83%, a value reasonably consistent with the $\chi_M T \approx 0.83$ cm^3 K mol^{-1} at 110 K, which corresponds to 78.2% of the HS-to-LS transformation. The angular distortion of [FeN$_6$] from the ideal octahedron, defined as the sum of the angular deviation of the 12 *cis* angles $\left(\Sigma = \sum_{1}^{12} \theta - 90 \right)$ is very similar for the two sites Σ_{Fe1} = 39.9° (110 K) and 58.2° (250 K) and Σ_{Fe2} = 44.5° (110 K) and 52.3° (250 K).

The only one [FeN$_6$] octahedral site found for **2** is characterized by ⟨Fe–N⟩ = 1.985(4) and 2.172(5) Å at 120 and 240 K, respectively. The difference of 0.187 Å well-corresponds with the change of the average Fe–N bond length typically observed for a complete HS ↔ LS transformation in agreement with the magnetic data. Furthermore, the SCO is accompanied by a change of Σ_{Fe} from 47.3° (120 K) to 60.1° (240 K). For **3·1/2CH$_2$Cl$_2$** the ⟨Fe–N⟩ value is 2.181(4) Å at 220 K, where the complex is fully HS and decreases down to ⟨Fe–N⟩ = 2.103(4) Å

at 120 K, the lowest attained temperature due to experimental limitations. The difference of 0.078 Å, consistent with a partial HS → LS transformation *ca.* 42%, matches reasonably well with the $\chi_M T$ value 2.3 cm^3 K mol^{-1} at 120 K, which corresponds *ca.* 40% of the complete HS → LS spin state change. In this interval of temperatures, Σ_{Fe} changes from 40.4° (120 K) to 52.1° (220). For the unsolvate form **3**, the ⟨Fe–N⟩ value equal to 2.184(4) Å at 120 K is perfectly consistent with the HS shown by this compound at any temperature, in spite of the Σ_{Fe} = 42.9°. However, at molecular level, the most remarkable difference between the structure of **3** and its solvated homologue is the different relative conformation of the two [H$_2$B(pz)$_2$]$^-$ ligands around the Fe^{II} centre (see Fig. 3). This difference makes the separation between the [H$_2$B(pz)$_2$]$^-$ tetrahedrons significantly longer for **3** (6.585 Å) than for its solvate counterpart (4.607 Å). This "short" conformation is also observed for **2**, while the "long" conformation is observed for **1·CH$_3$CN** as well as for the previously reported 2,2′-bipy and phen derivatives.

The crystal packing of **1·CH$_3$CN** is depicted in Fig. 4a. The unit cell contains four molecules, two for each crystallographically distinct Fe^{II} centre. Similar to the {Fe[H$_2$B(pz)$_2$]$_2$(phen)}[15–17] complex, the aromatic nature of the tzpy ligand enables the formation of a very efficient π–π stacking, involving a great number of intermolecular C···C contacts smaller than the sum of the van der Waals radii (≈3.7 Å) between adjacent complexes with alternating Fe1–Fe2–Fe1 centres running along the *a*-direction (Fig. 4b). The resulting supramolecular zig–zag chains stack down the *b*-direction, where no relevant interactions exist, defining layers parallel to the *a*–*b* plane, which stack along the *c*-direction generating voids where the CH$_3$CN molecules are located. Interestingly, the CH$_3$CN methyl group interacts with one of the pyrazole rings of each Fe1 and Fe2 centres (Fig. 4c). The number and the length of these short contacts strongly depend on the spin state of the compound (see Table S7, ESI†).

The non-aromatic nature of the neutral α-diimine ligand btz is the cause of the much less compact molecular packing exhibited by **2**. Indeed, no relevant intermolecular contacts are observed for this compound even in the LS state at 120 K
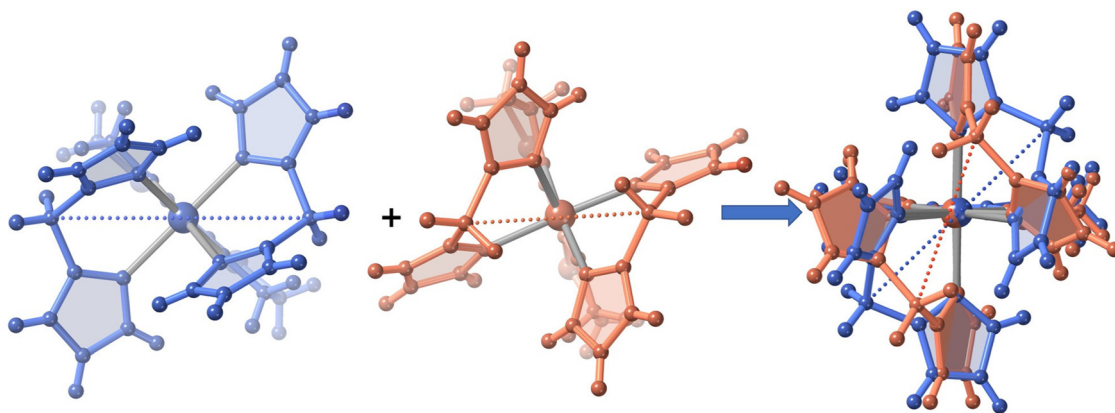
Fig. 3 Superposition of the isomeric {Fe[H$_2$B(pz)$_2$]$_2$(bt)} complexes from **3** (blue color) and **3·1/2CH$_2$Cl$_2$** (salmon color) denoting the different conformations of the [H$_2$B(pz)$_2$]$^-$ ligands around the Fe^{II} centres (see text). The dotted lines visually show the distinct separation between the B tetrahedral centres of [H$_2$B(pz)$_2$]$^-$.
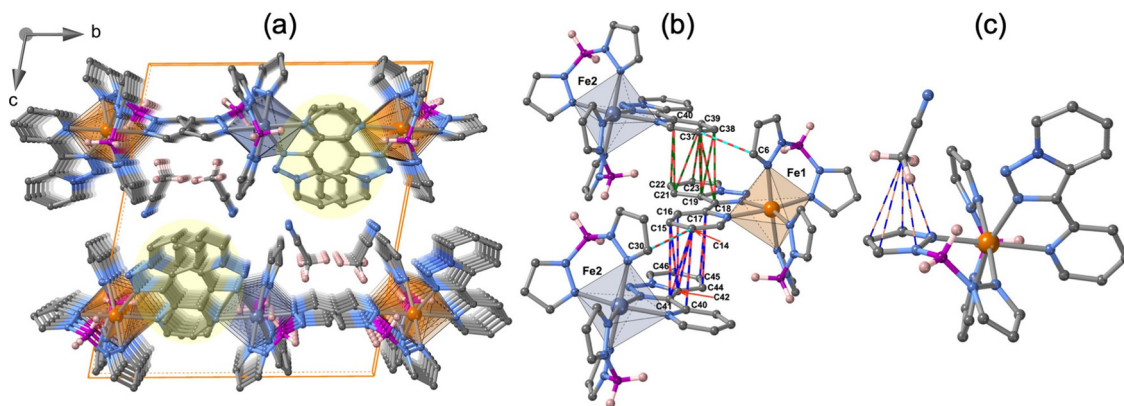
Fig. 4 (a) Crystal packing of **1·CH₃CN** denoting the alternating Fe1 and Fe2 sites as orange and blue octahedrons. The strong π–π interactions are marked within a filled yellow circle. (b) Fragments of the supramolecular chains held together through strong π–π interactions. (c) Intermolecular interaction between the NCCH₃···pyrazole. Thin bicolor red-green/red-blue/blue-pink bonds represent the interatomic contacts smaller than the sum of the van der Waals radii.

(Fig. S4 and Table S8, ESI†). In contrast, the crystal packing of **3·1/2CH₂Cl₂** and **3** displays a larger number of intermolecular C···C and C···S contacts, particularly at 120 K, despite bt also being a non-aromatic ligand (Fig. S5 and Table S8, ESI†).

Sublimation of 1 and 2 as molecular thin films

Thin films **TF1** and **TF2** ca. 200 nm thick were prepared by sublimation under HV conditions of the respective as-synthesized desolvated bulk powders **1** and **2** (see Methods). Also, sublimation of **3** was explored unsuccessfully since the bulk powder decomposed in the crucible upon heating without

accomplishing any deposition onto overlaying substrates. Different substrates (SiO₂, Au coated (40 nm) glass and CVD-graphene) were used for the deposition of the molecular films depending on their purpose. It is important to note that in this thickness range, the chemical integrity of SCO molecules is usually preserved for this family of compounds since surface-induced effects have only been observed in the (sub)monolayer regime.[23,26,27,29,56–58] Furthermore, all films show similar morphology, regardless of the type of substrate used, with highly homogenous coverages and very low roughness (ca. 1 nm), according to optical and atomic force microscopies (AFM) (Fig. 5). These results match with the characteristics observed
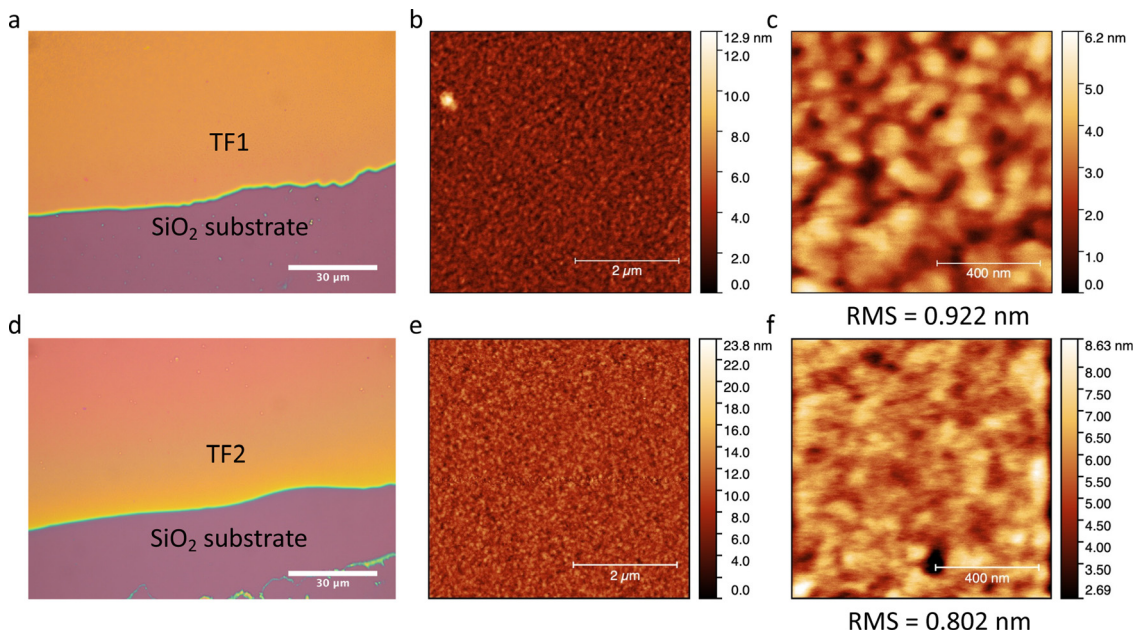
Fig. 5 Optical microscopy image (a), AFM image of 5 μm × 5 μm area (b) and AFM image of 1 μm × 1 μm area (c) collected on **TF1** deposited on SiO₂. Optical microscopy image (d), AFM image of 5 μm × 5 μm area (e) and AFM image of 1 μm × 1 μm area (f) collected on **TF2** deposited on SiO₂. The calculated roughness of the films obtained as the RMS value is indicated below each respective AFM image in (c and f). The scale in (a and d) is 30 μm, in (b and e) is 2 μm and in (c and f) is 400 nm.

for the other reported materials of this family of compounds in this thickness regime.[25,29,56,57]

The chemical integrity of **TF1** and **TF2** was analyzed by means of infrared (IR) and Raman spectroscopies. Moreover, their respective bulk materials (**1** and **2**) were characterized simultaneously for comparison. The high resemblance observed between the IR spectra of **TF1** and **TF2** grown on Au substrates, and those of their respective bulk powders **1** and **2**, stand out as an indicative feature of the preservation of the chemical integrity of the molecules after their sublimation.[24] Note in particular the characteristic vibrational modes of the asymmetrical/symmetrical stretching of the B–H bond: 2407/ 2283 cm^{-1} (**1**) and 2403/2283 cm^{-1} (**2**) (Fig. 6a and b). Similarly, the Raman spectra recorded using a 532 nm laser for **TF1** and **TF2** grown on SiO$_2$ substrates using two different laser powers show high similarity to those of **1** and **2** (Fig. 6c and d), evidencing retainment of the molecular integrity of the SCO molecules after sublimation, like other systems of the same family of SCO molecules.[57]

Spin crossover behavior of the deposited films TF1 and TF2 on SiO$_2$ and graphene substrates

The SCO behavior of the films **TF1** and **TF2** deposited on SiO$_2$ substrates, as well as that of their bulk counterparts **1** and **2**, was monitored using the XAS technique at the Fe L$_{2,3}$ edges (see Fig. 7). In order to get the thermally induced SCO profile of the films, temperature variable XAS spectra were recorded in both cooling and heating modes. Additional XAS spectra were recorded to characterize the LIESST effect irradiating the films for 10 min at 2 K using a red laser (λ = 633 nm) and the subsequent thermal relaxation of the photo-generated HS molecules upon heating in the dark. Concerning the bulk powders, only temperature variable XAS spectra were recorded in the cooling mode.

Upon cooling, the almost disappearance of the peaks found at 708.1 and 708.9 eV of the Fe L$_3$ edge at high temperature (characteristic of HS state) in favor of the appearance of a very intense new peak at 709.6 eV at low temperature (characteristic of LS state) in **1** and **2** is consistent with the thermal spin transition (Fig. 7a, b, g and h).[24,26,27,58,59] Furthermore, this is accompanied by a drastic increase in the intensity of the main peak of the Fe L$_2$ edge at 721.5 eV. Therefore, the thermal dependence of the HS fraction for **1** and **2** was obtained for the cooling mode from a linear fitting of the XAS spectra of the fully populated HS and LS states (see Fig. 7c and i). These thermal dependences characterized by $T_{1/2} \approx$ 170 and 195 K, for **1** and **2**, respectively, are fully consistent with the cooling branches derived from the magnetic susceptibility measurements (Fig. 1a and b).
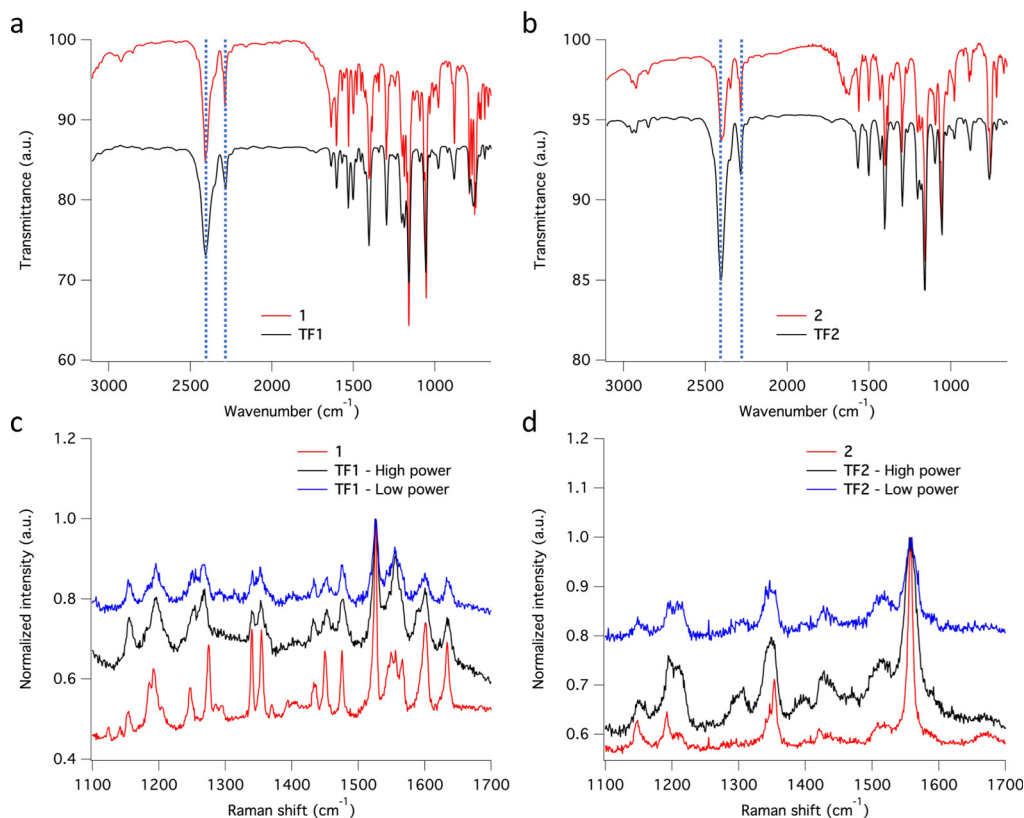
Fig. 6 IR spectra recorded for (a) **1** embedded in a KBr pellet (red line) and **TF1** deposited on Au (black line) and (b) **2** embedded in a KBr pellet (red line) and **TF2** deposited on Au (black line). Raman spectra recorded for (c) **1** scattered on a glass slide (red line – using a power of 20 μW μm^{-2}) and **TF1** deposited on SiO$_2$ (black line – using a laser power of 108 μW μm^{-2} and blue line – using a laser power of 11 μW μm^{-2}) and (d) **2** scattered on a glass slide (red line – using a power of 20 μW μm^{-2}) and **TF2** deposited on SiO$_2$ (black line – using a laser power of 108 μW μm^{-2} and blue line - using a laser power of 11 μW μm^{-2}).

Fig. 7 XAS spectra recorded at 250 and 100 K in the Fe (a) L_3 and (b) L_2 edges energy range for **1** scattered on C-tape and (c) calculated relative change from XAS spectra recorded at each temperature for a cooling process in a temperature range varying from 250 to 100 K in 10 K steps. XAS spectra recorded at 300, 80 and 2 K during a cooling process, 2 K after 10 min of 633 nm laser irradiation, and 80 K during a heating process in the Fe (d) L_3 and (e) $L_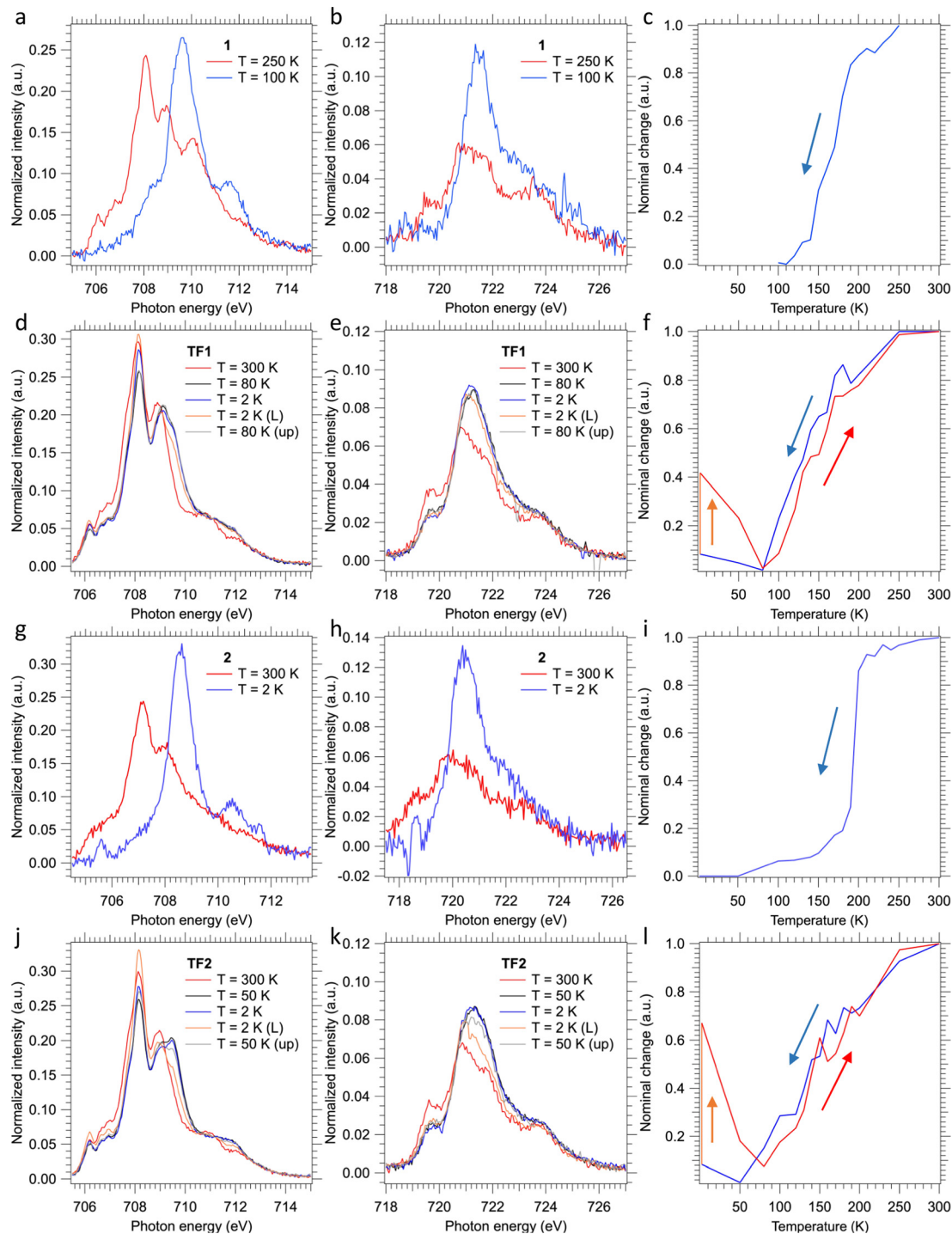2$ edges energy range for **TF1** deposited on SiO_2 and (f) calculated relative change from XAS spectra recorded at each temperature for cooling (blue line), 10 min of 633 nm laser irradiation (orange line) and heating (red line) processes in a temperature range including 300, 250, and 220 K, a temperature ramp between 200 and 120 K in 10 K steps, and 100, 80, 50 and 2 K (before and after irradiation). XAS spectra recorded at 300 and 2 K in the Fe (g) L_3 and (h) L_2 edges energy range for **2** scattered on C-tape and (i) calculated relative change from XAS spectra recorded at each temperature for a cooling process in a temperature range including 300, 275, and 250 K, a temperature ramp between 240 and 140 K in 10 K steps, and 120, 100, 50 and 2 K. XAS spectra recorded at 300, 50 and 2 K during a cooling process, 2 K after 10 min of 633 nm laser irradiation, and 50 K during a heating process in the Fe (j) L_3 and (k) L_2 edges energy range for **TF2** deposited on SiO_2 and (l) calculated relative change from XAS spectra recorded at each temperature for cooling (blue line), 10 min of 633 nm laser irradiation (orange line) and heating (red line) processes in a temperature range including 300, 250, and 220 K, a temperature ramp between 200 and 120 K in 10 K steps, and 100, 80, 50 and 2 K (before and after irradiation).

8114 | *J. Mater. Chem. C*, 2023, **11**, 8107–8120

This journal is © The Royal Society of Chemistry 2023

Nonetheless, the measured spectra also reveal partial oxidation of the bulk material since some contribution of Fe^{III} is observed at the Fe L$_3$ edge at 710 eV invariably at all temperatures.[60] Further evidence is found at the Fe L$_2$ edge, where its shape corroborates this partial oxidation of the bulk material.[60] This observation is in strong contrast with the magnetic susceptibility measurements, since no oxidation is observed for neither compound as the low-temperature $\chi_M T$ values practically equal to zero are consistent with 100% of Fe^{II} centres in both derivatives. Hence, we believe that this partial oxidation is the consequence of the unavoidable manipulation and adhesion of the bulk powders onto the C-tape for the performance of the XAS experiment.

Regarding thin films, the recorded XAS spectra at 300 K show a pure HS-Fe^{II} signal for both TF1 and TF2 films (red lines in Fig. 7d, e and j, k, respectively). The lack of oxidation in this case is accomplished by keeping the films under an inert atmosphere during the whole process, something unavoidable for the bulk powders. Upon cooling, both films appear to undergo some changes at the Fe L$_{2,3}$ edges in a similar fashion to the above-described for the respective bulk powders. However, in this case, the total changes accomplished at low temperatures (80 K and 50 K for TF1 and TF2, respectively) are much smaller (black lines in Fig. 7d, e and j, k). These results indicate that the thermal spin transition undergone by the films is incomplete, more gradual (blue lines in Fig. 7f and l) and shifted to lower temperatures, with $(T_{1/2})^{down} \approx$ 130 and 140 K for TF1 and TF2, respectively. Note that the exact value of the minimum HS fraction reached cannot be calculated with exact accuracy since the partial oxidation of the bulk powder prevented from collecting reliable pure HS and LS referential spectra. Nonetheless, from similar reported XAS characterization of molecules of this family, we can estimate a maximum thermally achieved HS to LS conversion close to 20% for TF1 at 80 K and close to 25% for TF2 at 50 K.[24,26,27,58,59] Upon further cooling, both molecules appear to experience some soft X-ray induced excited spin state trapping (SOXIESST) effect during the collection of the respective XAS spectra (blue lines in Fig. 7d, e and j, k), reaching at 2 K ca. 8% of the initial HS state (blue lines in Fig. 7f – between 2 and 80 K – and Fig. 7l – between 2 and 50 K). This manifests the susceptibility of the films to soft X-rays at low temperatures (below 80 K for TF1 and 50 K for TF2), something expectable since the SOXIESST effect has been already observed for films of other molecules of this family.[26,27,58]

Furthermore, upon red laser irradiation at 2 K during 10 min, the LIESST effect is accomplished (orange lines in Fig. 7d, e and j, k). This is especially effective in the film TF2, where ca. 70% of the LS molecules switch to the photo-generated HS state (orange line in Fig. 7f), in contrast to the film TF1 in which 40% of the LS centres are excited (orange lines in Fig. 7l). The metastable photo-generated HS states relaxed back to the LS through smooth heating (grey lines in Fig. 7d, e and j, k). This progression is clearly monitored between 2 K and 80 K (red lines in Fig. 7f and l) reaching back the ground state at ca. 80 K. Then, upon further heating, the thermal spin transition of both films shows full reversibility describing a similar trend as the cooling process, almost without hysteresis (red lines in Fig. 7f and l).

SCO was also studied in hybrid interfaces formed by subliming 1 and 2 as thin films over graphene. Following a similar procedure to that recently reported by us,[36] horizontal devices were produced depositing TF1 and TF2 onto pre-contacted CVD-graphene. In these heterostructures, the resistive properties of the underlying CVD-graphene substrate are highly sensitive to the strain induced by the volume change associated with the spin state change of the anchored SCO layer.[35,36] The measurements of the transport properties of the devices as a function of temperature for a single full thermal cycle between 2 and 250 K are presented in Fig. 8. In both cases, a change in the resistance of graphene is observed in the SCO/graphene device that does not appear in pristine CVD-graphene devices.[36] Thus, upon cooling, a progressive increase in the resistance is observed in the range 50–160 K centered at ca. 100–120 K, in good agreement with XAS measurements. Upon heating, an
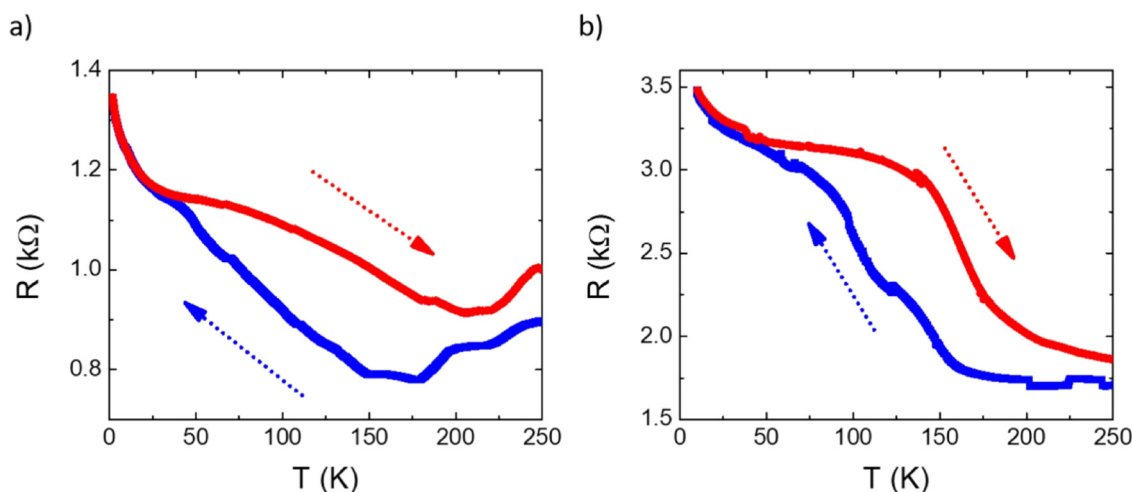

Fig. 8 Temperature dependence of the resistance in in-contact CVD-graphene horizontal devices integrating 200 nm thick films of (a) 1 and (b) 2 in the range between 2 and 250 K showing in blue the cooling process and in red the heating process.

This journal is © The Royal Society of Chemistry 2023

J. Mater. Chem. C, 2023, 11, 8107–8120 | 8115

apparent hysteretic behavior is observed. However, this behavior is not intrinsic to the material but due to the progressive loss of mass in the film under HV conditions, as can be seen by its overall thinning after the thermal cycling by *ca.* 25–30% (Fig. S6, ESI†). In fact, the cycling involves long measurement times (for example, a full cycle at 1 K min^{-1}, recording data every 0.5 K requires *ca.* 10 h), in such a manner that, under HV conditions, a part of the film sublimes back. Nonetheless, these results account for the successful electrical detection of the spin crossover transition in these films, corroborating the XAS experiment.

Conclusions

Sublimable spin crossover molecules are still very scarce. Here we have prepared novel molecules of this kind by extending the family {Fe[H$_2$B(pz)$_2$]$_2$(L)}, where L is a bidentate-α-diimine ligand. In the second step, we assess their suitability to be integrated as thin films into resistive devices. The three chosen bidentate α-diimine ligands, L = tzpy, btz and bt, have afforded the targeted complexes (**1–3**) plus two additional solvated forms (**1·CH$_3$CN**, **3·CH$_2$Cl$_2$**). All derivatives except **3·CH$_2$Cl$_2$** undergo thermal- and light-induced SCO behaviour with $T_{1/2}$ values in the range 115–200 K.

Sublimation of the two unsolvated SCO derivatives undergoing SCO properties, **1** and **2**, and subsequent controlled condensation of the molecules on specific substrates have afforded the corresponding 200 nm thick thin films **TF1** and **TF2** whose SCO properties have been characterized through XAS studies. From these XAS results, different features are observed in the SCO behavior that contrast with the expected as compared to the respective bulk powders: (i) the incomplete character of the thermal spin transition; (ii) the total loss of cooperativity; and (iii) the shifting to lower temperatures. Several circumstances may converge in the origin of these features. First, the high sensitivity of the films to X-ray irradiation is observed even at high temperatures (> 100 K). This effect could prevent a large fraction of the molecules from properly undergoing the thermal spin transition, as it has been previously observed in some bulk SCO materials and more recently for films of a SCO molecule, where the thermal spin transition was totally supressed.[36,61] Thus, since both films **TF1** and **TF2** show the typical SOXIESST effect up to 80 K and having a rather strong shifting to lower temperatures of their thermal spin transition, it could be reasonable to consider this high sensitivity to X-ray irradiation as a possible cause. A second additional explanation may arise from the very small size of nanoparticles in the film, not distinguishable in the AFM images collected (Fig. 1b, c, e and f), and the presence of defects, pinning some of these molecules in the HS state regardless of the temperature.[56–58,62] A partial decomposition of the pristine molecules on the surface to form tetrahedral (SCO inactive) [Fe(bpz)$_2$] fragments could also be considered.[27,58] However, since this fragmentation is only expected to occur at the (sub)monolayer level and would also affect substantially the shape of the XAS spectra at the Fe L$_{2,3}$ edge, this can be discarded in our case.

Finally, we have integrated these films **TF1** and **TF2** onto CVD-graphene based horizontal hybrid devices and detected their thermal SCO transition through the changes observed in the electrical properties of the underlying 2D material.

Methods

Synthesis

The ligands tzpy, btz and bt were synthesized according to methods previously described.[63,64] The potassium salt of the hydrobispyrazolylborate, K[H$_2$B(pz)$_2$], was purchased from commercial sources.

Synthesis of {Fe[H$_2$B(pz)$_2$]$_2$(L)}. All operations were performed in an Ar atmosphere. To a methanolic solution of K[H$_2$B(pz)$_2$] (4 mL, 98 mg, 0.526 nmol) prepared in a small Schlenk flask was added a colourless methanolic solution of Fe(ClO$_4$)$_2$·xH$_2$O ($x \approx 6$) (2 mL, 100 mg., 0.263 mmol) containing some crystals of ascorbic acid dissolved. After stirring for 10 min, a white-greyish powder appears (KClO$_4$) which was filtered off using a cannula under anaerobic conditions. Then, once transferred the resulting colourless solution 1Fe^{II}:2[H$_2$B(pz)$_2$]$^-$ in a larger Schlenk flask, a methanolic solution (4 mL) containing 0.263 mmol of L (tzpy, 51.4 mg; btz, 52.7 mg; bt, 45.24 mg) was added under continuous stirring. The tzpy derivative precipitated rapidly affording a pink-yellow microcrystalline powder, which corresponds to the unsolvated form **1**. In contrast, single crystals of the unsolvated forms of the btz (**2**) and bt (**3**) derivatives were obtained from evaporation of the resulting dark-blue mother liquor under argon flow in 24 h. Anal. calcd for C$_{23}$H$_{24}$N$_{12}$B$_2$Fe (**1**): C, 50.60; H, 4.43; N, 30.78. Found: C, 51.26; H, 4.48; N, 31.18. Anal. calcd for C$_{20}$H$_{28}$N$_{10}$B$_2$S$_2$Fe (**2**): C, 43.67; H, 5.13; N, 25.46. Found: C, 44.07; H, 5.20; N 25.73. Anal. calcd for C$_{18}$H$_{24}$N$_{10}$B$_2$S$_2$Fe: C, 41.41; H, 4.63; N, 26.83. Found: C, 41.65; H 4.52,; N 27.12.

Single crystals of **1·CH$_3$CN** were obtained by slow liquid diffusion (layering method) using test tubes containing a MeOH solution (3mL) of 1Fe^{II}/2[H$_2$Bpz$_2$]$^-$ at the bottom, a 1MeOH:1CH$_3$CN mixture (10 mL) in the middle and a CH$_3$CN solution (2 mL) of tzpy on top. Single crystals of **3·1/2CH$_2$Cl$_2$** were accidentally obtained trying to improve the yield of **3**. The synthetic protocol was modified replacing MeOH with CH$_2$Cl$_2$ as a solvent and keeping the resulting mother liquor in an ice bath during its slow evaporation in an argon stream. The crystals of **1·CH$_3$CN**, **2**, **3** and **3·1/2CH$_2$Cl$_2$** were analyzed using single crystal X-ray diffraction methods. The solvated compounds were also confirmed through thermogravimetric analysis.

Thin film sublimation. Thin films **TF1** and **TF2** were prepared by sublimation under high vacuum (HV) conditions of the as-synthesized and desolvated bulk powder of each of the molecules (**1** and **2** respectively, *ca.* 100 mg). For the film processing, these precursors were, respectively, introduced in quartz crucibles inside Knudsen cells fitting in our customized evaporation chamber (CREATEC Molecular Beam Epitaxy (MBE) customized system in a Clean Room Class 10 000). The sublimation conditions consisted in: (a) **1** heated at 100 °C in a 5 × 10^{-7} mbar HV to reach a deposition rate of 0.4 Å s^{-1}; and

8116 | *J. Mater. Chem. C*, 2023, **11**, 8107–8120

This journal is © The Royal Society of Chemistry 2023

(b) **2** heated at 90 °C in a 5×10^{-6} mbar HV to reach a deposition rate of 0.4 Å s^{-1}. These deposition rates were monitored by *in situ* sublimation through a calibrated quartz crystal microbalance (QCM), and the final thicknesses of the produced films (200 nm thick) were verified by profilometry (KLA Alpha-Step D-500 profilometer with a nanometric resolution).

Physical characterization

Elemental analyses (C, H, and N) were performed using a CE Instruments EA 1110 CHNS Elemental analyzer. Magnetic measurements were performed using a Quantum Design MPMS-XL-5 SQUID magnetometer in the 2 to 400 K temperature range with an applied magnetic field of 1 T. Experimental magnetic susceptibilities were corrected for diamagnetism of the constituent atoms by the use of Pascal's constants. Photomagnetic measurements were performed irradiating with a Diode Pumped Solid State Laser DPSS-532-20 from Chylas and coupled *via* an optical fiber to the cavity of the SQUID magnetometer. The optical power at the sample surface was adjusted to ~3 mW cm^{-2}, and it was verified that it resulted in no significant change in magnetic response due to heating of the sample. The samples consisted of a thin layer of the compound whose weight was corrected by comparison of a thermal spin crossover curve with that of a more accurately weighted sample of the same compound. Calorimetric measurements were performed using a differential scanning calorimeter Mettler Toledo DSC 821e. Low temperatures were obtained with an aluminium block attached to the sample holder, refrigerated with a flow of liquid nitrogen and stabilized at a temperature of 110 K. The sample holder was kept in a dry box under a flow of dry nitrogen gas to avoid water condensation. The measurements were carried out using around 10–15 mg of polycrystalline samples sealed in aluminium pans with a mechanical crimp. Temperature and heat flow calibrations were made using standard samples of indium using its melting transition (429.6 K, 28.45 J g^{-1}). An overall accuracy of ±0.2 K in temperature and ±2% in the heat capacity is estimated. The uncertainty increases for the determination of the anomalous enthalpy and entropy due to the subtraction of an unknown baseline. Powder X-ray measurements were performed on a PANalytical Empyrean X-ray powder diffractometer (monochromatic CuKα radiation).

Single crystal X-ray measurements. Single crystals were mounted on a glass fiber using viscous hydrocarbon oil to coat the crystal and then transferred directly to the cold nitrogen stream for data collection. X-Ray data were collected on an Oxford Diffraction Supernova diffractometer equipped with a graphite-monochromated Enhance (Mo) X-Ray Source (λ = 0.71073 Å). The program CrysAlisPro, Oxford Diffraction Ltd, was used for unit cell determinations and data reduction. Empirical absorption correction was performed using spherical harmonics, implemented in the SCALE3 ABSPACK scaling algorithm. The structures were solved by direct methods and refined by full matrix least-squares on F^2 using SHELXL-2018.[65] Non-hydrogen atoms were refined anisotropically, and hydrogen atoms were placed in calculated positions refined using

idealized geometries (riding model) and assigned fixed isotropic displacement parameters.†

Thin film characterization. Optical microscopy images were collected using a Nikon Eclipse LV-150N microscope equipped with a Nikon DS-FI3 camera through a 100× objective. Atomic Force Microscopy (AFM) images for **TF1** and **TF2** were collected using a Bruker Dimension Icon with Scan Assyst in a tapping mode in 1 μm × 1 μm and 5 μm × 5 μm areas. These images were processed using Gwyddion software, from which the roughness of the films was obtained as the Root Mean Square statistical value (RMS). Infrared Spectroscopy: IR spectra were recorded using a Fourier Transformation-Infrared Spectrometer NICOLET 5700 from Thermo Electron Corporation in the wavenumber range between 3100 cm^{-1} and 650 cm^{-1}. For **TF1** and **TF2**, grown on 3 cm × 3 cm Au coated glass substrates, a module was used that allowed the measurement of the transmittance of the reflected IR light from the sample. In the case of the respective bulk powders, embedded in KBr pellets, a second module was used that allowed the measurement of transmittance of IR light after going through the KBr pellets separately containing **1** and **2** dispersed molecular materials. Raman Spectroscopy: Raman spectra were recorded on **TF1** and **TF2** grown on 7 mm × 7 mm SiO$_2$ substrates and on **1** and **2** scattered powders on a glass slide using a Horiba LabRAM HR Evolution spectrometer equipped with a 532 nm Laser beam with a maximum power of 1.08 mW μm^{-2}. The Raman shift in these spectra ranged between 1100 cm^{-1} and 1700 cm^{-1}. For the bulk powders, the power used during the data collection was of 20 μW μm^{-2}. In the case of the films, spectra with two different laser powers were recorded: (a) 11 μW μm^{-2} and (b) 109 μW μm^{-2}.

X-Ray absorption spectroscopy. XAS characterization of **TF1** and **TF2** deposited on 7 mm × 3 mm Si/SiO$_2$ substrates and of **1** and **2** bulk powders was performed at Boreas beamline in ALBA synchrotron. The films were attached to copper sample holders using aluminum clips and placing an indium foil below to improve their thermalization. Bulk powders were scattered onto C-tape placed directly on top of copper sample holders. The measurements implied the collection of several energy scans focused at the Fe L$_{2,3}$ edge region at different temperatures onto each sample, cooling and heating processes for the films and only cooling for the powders. These scans were performed using a total electron yield mode and substantially low photon flux (intensity $\leq$ 0.025 nA) with a sufficient signal to noise ratio. Moreover, all samples were only irradiated with X-rays during the spectral collection, only exposing them during these periods to prevent as much as possible unwilled/avoidable X-ray induced phenomena. For the LIESST effect study on the films, these were irradiated using a red laser (He–Ne LASER from Research Electro-optics Inc. (R-30993), wavelength 633 nm and power 12 mW) at 2 K, right after the cooling process, for 10 min. All recorded spectra for this study were processed for their analysis through background subtraction and normalization. The evolution of the spectra recorded for each case with temperature was studied, respectively, as a relative change from its fitting to a linear combination of the

This journal is © The Royal Society of Chemistry 2023

J. Mater. Chem. C, 2023, **11**, 8107–8120 | 8117

spectra showing the highest (1 in the plots) and lowest (0 in the plots) HS fraction, respectively.

Device fabrication and electrical characterization. Both device fabrication and electrical characterization were performed following the methods described in our previous work for in-contact devices but using the SCO molecules described in the present text with their respective sublimation conditions.[36]

Conflicts of interest

There are no conflicts to declare.

Acknowledgements

References

1 E. König, *Environmental Science and Technology*, 1991, vol. 43, pp. 51–152.

2 P. Gütlich, A. Hauser and H. Spiering, *Angew. Chem., Int. Ed. Engl.*, 1994, **33**, 2024–2054.

3 J. A. Real, A. B. Gaspar, V. Niel and M. C. Muñoz, *Coord. Chem. Rev.*, 2003, **236**, 121–141.

4 P. Gütlich and H. A. Goodwin, *Spin Crossover in Transition Metal Compounds I*, Springer Berlin Heidelberg, Berlin, Heidelberg, 2004, vol. 233.

5 P. Gütlich and H. A. Goodwin, *Spin Crossover in Transition Metal Compounds II*, Springer Berlin Heidelberg, Berlin, Heidelberg, 2004, vol. 234.

6 P. Gütlich and H. A. Goodwin, *Spin Crossover in Transition Metal Compounds III*, Springer Berlin Heidelberg, Berlin, Heidelberg, 2004, vol. 235.

7 J. A. Real, A. B. Gaspar and M. C. Muñoz, *Dalton. Trans.*, 2005, 2062.

8 A. Bousseksou, G. Molnár, L. Salmon and W. Nicolazzi, *Chem. Soc. Rev.*, 2011, **40**, 3313.

9 W. Nicolazzi and A. Bousseksou, *Comptes Rendus Chim.*, 2018, **21**, 1060–1074.

10 G. Molnár, S. Rat, L. Salmon, W. Nicolazzi and A. Bousseksou, *Adv. Mater.*, 2018, **30**, 1703862.

11 K. S. Kumar and M. Ruben, *Angew. Chem., Int. Ed.*, 2021, **60**, 7502–7521.

12 E. König and K. Madeja, *Inorg. Chem.*, 1967, **6**, 48–55.

13 W. A. Baker and H. M. Bobonich, *Inorg. Chem.*, 1964, **3**, 1184–1188.

14 B. Gallois, J. A. Real, C. Hauw and J. Zarembowitch, *Inorg. Chem.*, 1990, **29**, 1152–1158.

15 J. A. Real, M. C. Muñoz, J. Faus and X. Solans, *Inorg. Chem.*, 1997, **36**, 3008–3013.

16 N. Moliner, L. Salmon, L. Capes, M. C. Muñoz, J.-F. Létard, A. Bousseksou, J.-P. Tuchagues, J. J. McGarvey, A. C. Dennis, M. Castro, R. Burriel and J. A. Real, *J. Phys. Chem. B*, 2002, **106**, 4276–4283.

17 A. L. Thompson, A. E. Goeta, J. A. Real, A. Galet and M. Carmen Muñoz, *Chem. Commun.*, 2004, 1390–1391.

18 J. P. Jesson, J. F. Weiher and S. Trofimenko, *J. Chem. Phys.*, 1968, **48**, 2058–2066.

19 V. Davesne, M. Gruber, T. Miyamachi, V. Da Costa, S. Boukari, F. Scheurer, L. Joly, P. Ohresser, E. Otero, F. Choueikani, A. B. Gaspar, J. A. Real, W. Wulfhekel, M. Bowen and E. Beaurepaire, *J. Chem. Phys.*, 2013, **139**, 074708.

20 S. Shi, G. Schmerber, J. Arabski, J.-B. Beaufrand, D. J. Kim, S. Boukari, M. Bowen, N. T. Kemp, N. Viart, G. Rogez, E. Beaurepaire, H. Aubriet, J. Petersen, C. Becker and D. Ruch, *Appl. Phys. Lett.*, 2009, **95**, 043303.

21 M. Gruber, T. Miyamachi, V. Davesne, M. Bowen, S. Boukari, W. Wulfhekel, M. Alouani and E. Beaurepaire, *J. Chem. Phys.*, 2017, **146**, 092312.

22 T. G. Gopakumar, F. Matino, H. Naggert, A. Bannwarth, F. Tuczek and R. Berndt, *Angew. Chem., Int. Ed.*, 2012, **51**, 6262–6266.

23 E. Ludwig, H. Naggert, M. Kalläne, S. Rohlf, E. Kröger, A. Bannwarth, A. Quer, K. Rossnagel, L. Kipp and F. Tuczek, *Angew. Chem., Int. Ed.*, 2014, **53**, 3019–3023.

24 H. Naggert, J. Rudnik, L. Kipgen, M. Bernien, F. Nickel, L. M. Arruda, W. Kuch, C. Näther and F. Tuczek, *J. Mater. Chem. C*, 2015, **3**, 7870–7877.

25 C. Lefter, S. Rat, J. S. Costa, M. D. Manrique-Juárez, C. M. Quintero, L. Salmon, I. Séguy, T. Leichle, L. Nicu, P. Demont, A. Rotaru, G. Molnár and A. Bousseksou, *Adv. Mater.*, 2016, **28**, 7508–7514.

26 M. Bernien, H. Naggert, L. M. Arruda, L. Kipgen, F. Nickel, J. Miguel, C. F. Hermanns, A. Krüger, D. Krüger, E. Schierle, E. Weschke, F. Tuczek and W. Kuch, *ACS Nano*, 2015, **9**, 8960–8966.

27 S. Ossinger, H. Naggert, L. Kipgen, T. Jasper-Toennies, A. Rai, J. Rudnik, F. Nickel, L. M. Arruda, M. Bernien, W. Kuch, R. Berndt and F. Tuczek, *J. Phys. Chem. C*, 2017, **121**, 1210–1219.

8118 | *J. Mater. Chem. C*, 2023, **11**, 8107–8120

This journal is © The Royal Society of Chemistry 2023

28 A. Pronschinske, Y. Chen, G. F. Lewis, D. A. Shultz, A. Calzolari, M. Buongiorno Nardelli and D. B. Dougherty, *Nano Lett.*, 2013, **13**, 1429–1434.

29 A. Pronschinske, R. C. Bruce, G. Lewis, Y. Chen, A. Calzolari, M. Buongiorno-Nardelli, D. A. Shultz, W. You and D. B. Dougherty, *Chem. Commun.*, 2013, **49**, 10446–10452.

30 X. Zhang, P. S. Costa, J. Hooper, D. P. Miller, A. T. N'Diaye, S. Beniwal, X. Jiang, Y. Yin, P. Rosa, L. Routaboul, M. Gonidec, L. Poggini, P. Braunstein, B. Doudin, X. Xu, A. Enders, E. Zurek and P. A. Dowben, *Adv. Mater.*, 2017, **29**, 1702257.

31 L. Kipgen, M. Bernien, S. Ossinger, F. Nickel, A. J. Britton, L. M. Arruda, H. Naggert, C. Luo, C. Lotze, H. Ryll, F. Radu, E. Schierle, E. Weschke, F. Tuczek and W. Kuch, *Nat. Commun.*, 2018, **9**, 2984.

32 K. S. Kumar, M. Studniarek, B. Heinrich, J. Arabski, G. Schmerber, M. Bowen, S. Boukari, E. Beaurepaire, J. Dreiser and M. Ruben, *Adv. Mater.*, 2018, **30**, 1705416.

33 V. Davesne, M. Gruber, M. Studniarek, W. H. Doh, S. Zafeiratos, L. Joly, F. Sirotti, M. G. Silly, A. B. Gaspar, J. A. Real, G. Schmerber, M. Bowen, W. Weber, S. Boukari, V. Da Costa, J. Arabski, W. Wulfhekel and E. Beaurepaire, *J. Chem. Phys.*, 2015, **142**, 194702.

34 O. Iasco, M.-L. Boillot, A. Bellec, R. Guillot, E. Rivière, S. Mazerat, S. Nowak, D. Morineau, A. Brosseau, F. Miserque, V. Repain and T. Mallah, *J. Mater. Chem. C*, 2017, **5**, 11067–11075.

35 N. Konstantinov, A. Tauzin, U. N. Noumbé, D. Dragoe, B. Kundys, H. Majjad, A. Brosseau, M. Lenertz, A. Singh, S. Berciaud, M.-L. Boillot, B. Doudin, T. Mallah and J.-F. Dayen, *J. Mater. Chem. C*, 2021, **9**, 2712–2720.

36 M. Gavara-Edo, R. Córdoba, F. J. Valverde-Muñoz, J. Herrero-Martín, J. A. Real and E. Coronado, *Adv. Mater.*, 2022, **34**, 2202551.

37 K. Bairagi, O. Iasco, A. Bellec, A. Kartsev, D. Li, J. Lagoute, C. Chacon, Y. Girard, S. Rousset, F. Miserque, Y. J. Dappe, A. Smogunov, C. Barreteau, M. L. Boillot, T. Mallah and V. Repain, *Nat. Commun.*, 2016, **7**, 12212.

38 K. Bairagi, A. Bellec, C. Fourmental, O. Iasco, J. Lagoute, C. Chacon, Y. Girard, S. Rousset, F. Choueikani, E. Otero, P. Ohresser, P. Sainctavit, M.-L. Boillot, T. Mallah and V. Repain, *J. Phys. Chem. C*, 2018, **122**, 727–731.

39 L. Zhang, Y. Tong, M. Kelai, A. Bellec, J. Lagoute, C. Chacon, Y. Girard, S. Rousset, M. Boillot, E. Rivière, T. Mallah, E. Otero, M. Arrio, P. Sainctavit and V. Repain, *Angew. Chem., Int. Ed.*, 2020, **59**, 13341–13346.

40 M. Kelai, B. Cahier, M. Atanasov, F. Neese, Y. Tong, L. Zhang, A. Bellec, O. Iasco, E. Rivière, R. Guillot, C. Chacon, Y. Girard, J. Lagoute, S. Rousset, V. Repain, E. Otero, M.-A. Arrio, P. Sainctavit, A.-L. Barra, M.-L. Boillot and T. Mallah, *Inorg. Chem. Front.*, 2021, **8**, 2395–2404.

41 Y. Tong, M. Kelaï, K. Bairagi, V. Repain, J. Lagoute, Y. Girard, S. Rousset, M.-L. Boillot, T. Mallah, C. Enachescu and A. Bellec, *J. Phys. Chem. Lett.*, 2021, **12**, 11029–11034.

42 M. Kelai, V. Repain, A. Tauzin, W. Li, Y. Girard, J. Lagoute, S. Rousset, E. Otero, P. Sainctavit, M.-A. Arrio, M.-L. Boillot,

T. Mallah, C. Enachescu and A. Bellec, *J. Phys. Chem. Lett.*, 2021, **12**, 6152–6158.

43 D. Li, Y. Tong, K. Bairagi, M. Kelai, Y. J. Dappe, J. Lagoute, Y. Girard, S. Rousset, V. Repain, C. Barreteau, M. Brandbyge, A. Smogunov and A. Bellec, *J. Phys. Chem. Lett.*, 2022, **13**, 7514–7520.

44 L. Salmon, G. Molnár, S. Cobo, P. Oulié, M. Etienne, T. Mahfoud, P. Demont, A. Eguchi, H. Watanabe, K. Tanaka and A. Bousseksou, *New J. Chem.*, 2009, **33**, 1283.

45 T. Mahfoud, G. Molnár, S. Cobo, L. Salmon, C. Thibault, C. Vieu, P. Demont and A. Bousseksou, *Appl. Phys. Lett.*, 2011, **99**, 053307.

46 S. Rat, K. Ridier, L. Vendier, G. Molnár, L. Salmon and A. Bousseksou, *CrystEngComm*, 2017, **19**, 3271–3280.

47 M. Bernien, D. Wiedemann, C. F. Hermanns, A. Krüger, D. Rolf, W. Kroener, P. Müller, A. Grohmann and W. Kuch, *J. Phys. Chem. Lett.*, 2012, **3**, 3431–3434.

48 M. Atzori, L. Poggini, L. Squillantini, B. Cortigiani, M. Gonidec, P. Bencok, R. Sessoli and M. Mannini, *J. Mater. Chem. C*, 2018, **6**, 8885–8889.

49 S. Rohlf, M. Gruber, B. M. Flöser, J. Grunwald, S. Jarausch, F. Diekmann, M. Kalläne, T. Jasper-Toennies, A. Buchholz, W. Plass, R. Berndt, F. Tuczek and K. Rossnagel, *J. Phys. Chem. Lett.*, 2018, **9**, 1491–1496.

50 C. Boix-Constant, V. García-López, E. Navarro-Moratalla, M. Clemente-León, J. L. Zafra, J. Casado, F. Guinea, S. Mañas-Valero and E. Coronado, *Adv. Mater.*, 2022, **34**, 2110027.

51 S. Decurtins, P. Gütlich, C. P. Köhler, H. Spiering and A. Hauser, *Chem. Phys. Lett.*, 1984, **105**, 1–4.

52 J.-F. Létard, P. Guionneau, L. Rabardel, J. A. K. Howard, A. E. Goeta, D. Chasseau and O. Kahn, *Inorg. Chem.*, 1998, **37**, 4432–4441.

53 A. Hauser, *Coord. Chem. Rev.*, 1991, **111**, 275–290.

54 A. Hauser, A. Vef and P. Adler, *J. Chem. Phys.*, 1991, **95**, 8710–8717.

55 A. Hauser, C. Enachescu, M. L. Daku, A. Vargas and N. Amstutz, *Coord. Chem. Rev.*, 2006, **250**, 1642–1652.

56 H. Naggert, A. Bannwarth, S. Chemnitz, T. Von Hofe, E. Quandt and F. Tuczek, *Dalton. Trans.*, 2011, **40**, 6364–6366.

57 T. Palamarciuc, J. C. Oberg, F. El Hallak, C. F. Hirjibehedin, M. Serri, S. Heutz, J. F. Létard and P. Rosa, *J. Mater. Chem.*, 2012, **22**, 9690–9695.

58 T. G. Gopakumar, M. Bernien, H. Naggert, F. Matino, C. F. Hermanns, A. Bannwarth, S. Mühlenberend, A. Krüger, D. Krüger, F. Nickel, W. Walter, R. Berndt, W. Kuch and F. Tuczek, *Chem. – Eur. J.*, 2013, **19**, 15702–15709.

59 B. Warner, J. C. Oberg, T. G. Gill, F. El Hallak, C. F. Hirjibehedin, M. Serri, S. Heutz, M. A. Arrio, P. Sainctavit, M. Mannini, G. Poneti, R. Sessoli and P. Rosa, *J. Phys. Chem. Lett.*, 2013, **4**, 1546–1552.

60 G. Cressey, C. M. B. Henderson and G. van der Laan, *Phys. Chem. Miner.*, 1993, **20**, 111–119.

61 A. Y. Mohamed, M. Lee, K. Kitase, T. Kitazawa, J. Y. Kim and D. Y. Cho, *Crystals*, 2018, **8**, 433.

62 C. Bartual-Murgui, V. Rubio-Giménez, M. Meneses-Sánchez, F. J. Valverde-Muñoz, S. Tatay, C. Martí-Gastaldo,

This journal is © The Royal Society of Chemistry 2023

J. Mater. Chem. C, 2023, **11**, 8107–8120 | 8119

M. C. Muñoz and J. A. Real, *ACS Appl. Mater. Interfaces*, 2020, **12**, 29461–29472.

63 V. Niel, A. B. Gaspar, M. C. Muñoz, B. Abarca, R. Ballesteros and J. A. Real, *Inorg. Chem.*, 2003, **42**, 4782–4788.

64 D. A. Tomalia and J. N. Paige, *J. Org. Chem.*, 1973, **38**, 3949–3951.

65 G. M. Sheldrick, *Acta Crystallogr., Sect. C: Struct, Chem*, 2015, **71**, 3–8.